CMS Physics Analysis Summary

Evidence for proton-tagged, central semi-exclusive production of high-mass muon pairs at 13 TeV with the CMS-TOTEM Precision Proton Spectrometer

The CMS and TOTEM Collaborations

Abstract

The process $pp \rightarrow p\mu^+\mu^- p^{(*)}$ has been observed at the LHC for dimuon masses larger than 110 GeV in pp collisions at $\sqrt{s} = 13$ TeV. Here $p^{(*)}$ indicates that the second proton is undetected, and either remains intact or dissociates into a low-mass state p^*. The scattered proton has been measured in the CMS-TOTEM Precision Proton Spectrometer (CT-PPS), which operated for the first time in 2016. The measurement is based on an integrated luminosity of approximately 10 fb^{-1} collected in regular, high-luminosity fills. A total of 12 candidates with $m(\mu\mu) > 110$ GeV, and matching forward proton kinematics, is observed. This corresponds to an excess of more than four standard deviations over the background. The spectrometer and its operation are described, along with the data and background estimation. The present results constitute the first evidence of this process at such masses. They also demonstrate that CT-PPS performs as expected.

1 Introduction

The present paper reports evidence of central semi-exclusive production of dimuon pairs, $pp \to p\mu^+\mu^- p^{(*)}$, with mass $m(\mu\mu) > 110$ GeV. The two muons are measured in the central CMS apparatus, and the final state proton in the CMS-TOTEM Precision Proton Spectrometer (CT-PPS). The latter is a near-beam magnetic spectrometer that uses the LHC magnets between the Interaction Point (IP) and detectors at about 210 m from the IP on both sides. Protons that have lost a small fraction of their momentum are bent out of the beam envelope so that their trajectories can be measured. The second proton may either remain intact or dissociate into a low mass state, indicated by the symbol p^*, and escapes undetected in the forward region opposite that of the measured proton.

Central dimuon production is dominated by the diagrams shown in Fig. 1, in which both protons radiate quasi-real photons that interact and produce the two muons. The left and center diagrams result in at least one intact final state proton, and are considered as signal in this analysis. However, the acceptance for detecting both protons starts only above $m(\mu\mu) \sim 400$ GeV, where the cross section for Standard Model $pp \to p\mu^+\mu^- p$ production is very small. By using events with only a single proton tagged, the final sample will contain a mixture of "elastic" (or "exclusive", $pp \to p\mu^+\mu^- p$) and single proton-dissociation ($pp \to p\mu^+\mu^- p^*$) events, but the acceptance is extended to lower masses where the cross section is non-negligible. The rightmost diagram is considered as a background. A background contribution is also expected from Drell-Yan events in which a proton from another interaction in the same bunch crossing (pileup) is wrongly associated to the dimuon system.
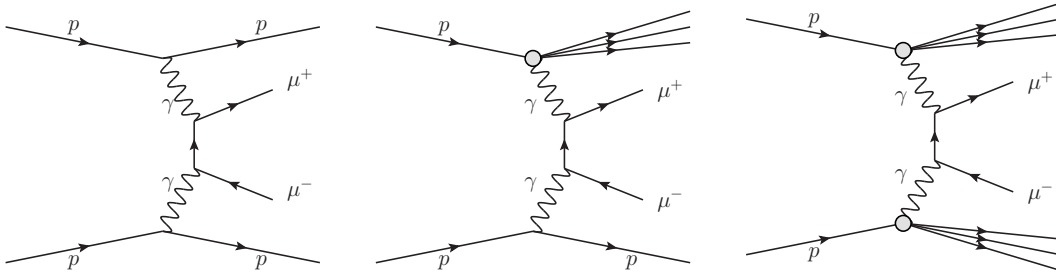

Figure 1: Production of muon pairs by $\gamma\gamma$ fusion. The "elastic" (left), single proton dissociation (center), and double proton dissociation (right) topologies are shown. The left and center diagrams result in at least one intact final state proton, and are considered as signal in this analysis. The rightmost diagram is considered as a background.

Central semi-exclusive dimuon production has never been measured directly and is of interest because it constitutes a background to the exclusive reaction $pp \to p\mu^+\mu^- p$ when the final-state protons are not measured. In turn, the exclusive process is interesting because deviations from the expected cross section, which is well known, may be an indication of new physics. In central semi-exclusive events, the momentum of the two muons can be used to determine that of the proton, and hence the proton fractional momentum loss ξ. This indirect measurement of ξ can be compared with the direct one obtained with CT-PPS. The comparison can be used to suppress background; it also provides proof of the correct functioning of CT-PPS and can be used to estimate its resolution.

CT-PPS operated for the first time in 2016 and collected a total of $\sim$15 fb^{-1} in regular, high-luminosity runs of LHC. For the present analysis, a sample of approximately 10 fb^{-1} is used; the remaining data were taken after September 2016, when LHC collided protons with a different crossing angle, which implies a different CT-PPS acceptance.

The paper is organized as follows: Section 2 describes the experimental set-up; Sections 3-4 illustrate the procedures to derive the alignment and LHC optics parameters from the data. Section 5 documents the samples of data and simulated events used in the analysis, while Sections 6 and 7 explain the event selection criteria, and the methods applied to estimate the backgrounds, respectively. Finally, the analysis and the results are presented in Section 8, followed by a summary in Section 9.

2   Experimental set-up

The central feature of the CMS apparatus is a superconducting solenoid of 6 m internal diameter, providing a magnetic field of 3.8 T. Within the solenoid volume are a silicon pixel and strip tracker, a lead tungstate crystal electromagnetic calorimeter (ECAL), and a brass and scintillator hadron calorimeter (HCAL), each composed of a barrel and two endcap sections. Forward calorimeters extend the pseudorapidity coverage provided by the barrel and endcap detectors. Muons are measured in gas-ionization detectors embedded in the steel flux-return yoke outside the solenoid. A more detailed description of the CMS detector, together with a definition of the coordinate system used and the relevant kinematic variables, can be found in Ref. [1].

The CMS-TOTEM Precision Proton Spectrometer [2] detects protons scattered at small angles and carrying a substantial fraction of the incoming beam momentum. These protons remain in the beam pipe and their trajectory is measured by a system of position sensitive detectors at a distance of about 210 m from the IP, on both sides of CMS. They are complemented by timing counters to measure the proton arrival time. The detector planes are inserted horizontally in the beam pipe by means of "Roman Pots" (RP), i.e. movable near-beam devices that allow bringing the detectors very close (down to a few mm) to the beam without affecting the accelerator vacuum.

The layout of the beam line from the IP to the 210 m region on one of the two sides of CMS is shown in Fig. 2. The two sides are referred to as "arms" in the following. The arm to the left of CMS when looking from the center of the LHC (positive z direction in the CMS coordinate system) corresponds to the LHC sector 45, and the one to the right to LHC sector 56. In each arm there are two tracking units, referred to as "210 near" (210N) and "210 far" (210F), at 203.8 m and 212.6 m from the IP, respectively. In 2016, the tracking RPs were instrumented with 10 planes of edgeless Si strip sensors each, providing a spatial resolution of about 12 μm. These pots as well as the sensors have been extensively used by TOTEM and are described in Ref. [3]. In order to operate at high luminosity, the RPs have been equipped with special ferrite shielding so as to reduce their electromagnetic impedance, and hence the impact on the LHC beams. The TOTEM Si strip sensors were not designed to sustain exposure to the high radiation doses of the regular high-luminosity LHC fills. Indeed, a first set of such planes underwent severe radiation damage after about 10 fb^{-1}, and was replaced by a set of spares. The timing detectors are housed in new, low-impedance, cylindical RPs specially built for CT-PPS, located at 215.7 m from the IP. They were equipped with diamond detectors for the last part of the run to complement the tracking Si strips. They are not used for the analysis discussed here. In its final configuration, CT-PPS will use 3D Si pixel sensors for tracking and a combination of diamond and Si sensors for timing.

The data used for the present paper were collected with the RPs at a distance of about 15 σ from the beam, where σ is the standard deviation of the spatial distribution of the beam in the transverse plane, which ranges from 0.245 mm for the 210N RP to 0.14 mm for the timing RP. Figure 3 shows a typical distribution of the track impact points in a RP at 15 σ.
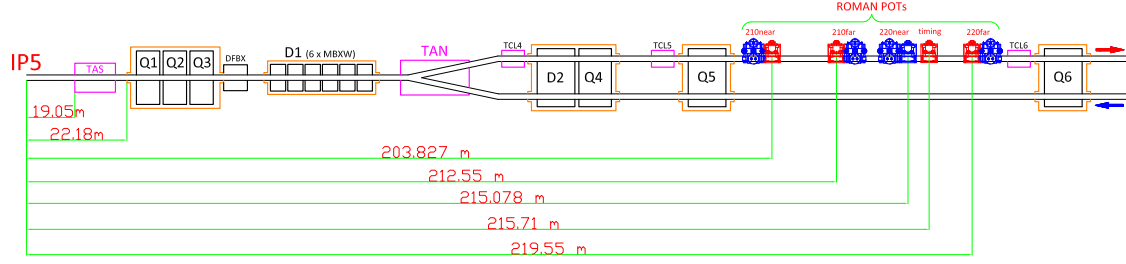
Figure 2: The layout of the beam line (seen from above) between the interaction point (IP5) and the region where the RPs are located in LHC sector 56. Dipoles (D1, D2), quadrupoles (Q1-Q6), collimators (TCL4-TCL6), as well as absorbers (TAS, TAN) are shown. The 210 near and 210 far units are indicated, along with the timing RPs. The 220 near and 220 far units (not used here) are also shown. The RPs indicated in red are the horizontal CT-PPS ones; those in blue belong to TOTEM. The red arrow indicates the outgoing beam, while the blue one the incoming beam. The arm in LHC sector 45 is symmetric with respect to the IP. The drawing is not to scale.
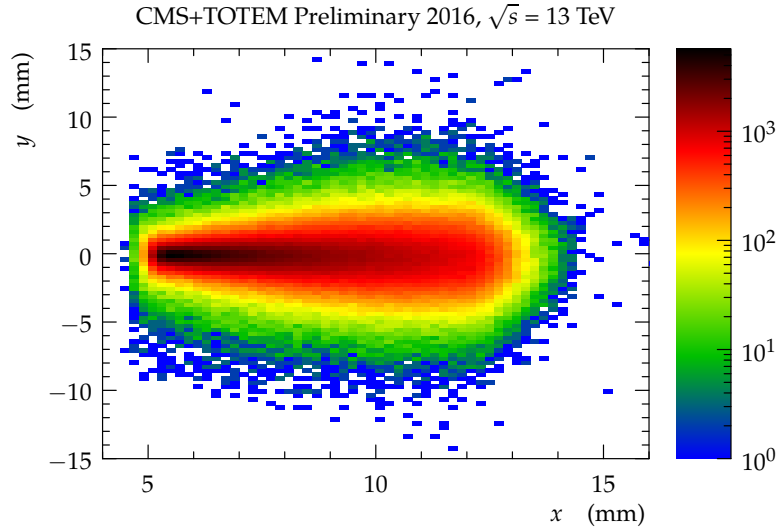
Figure 3: Example of track impact point distribution measured in RP 210F, sector 45, at 15 σ from the beam. The beam center is at $x = y = 0$.

3   Alignment

Alignment of CT-PPS is required in order to determine precisely the position of the sensors with respect to each other inside a RP, the relative position of the RPs, as well as the overall position of the spectrometer with respect to the beam. An overview of the procedure is given here; more details are available in Ref. [4].

The alignment consists of two conceptually distinct parts:

- Alignment in a special, low-luminosity calibration fill ("alignment fill"), where RPs are inserted very close to the beam (about 5 σ).
- Transfer of the alignment information to the standard, high-luminosity fills.

3.1 Alignment fill

The first step is the beam-based alignment, the purpose of which is to establish the position of the RPs with respect to the LHC collimators and the beam. It takes place only once per LHC optics setting. In this procedure, the TOTEM vertical RPs [3] (cf. Fig. 2) are used together with the horizontal CT-PPS RPs discussed in Section 2. The beam is first scraped with the collimators so that it acquires a sharp edge. Then each RP is moved in small (O(10 μm)) steps until it is in direct contact with the beam, which generates a rapid increase in the rate of beam-loss monitors close to CT-PPS. At this point, each RP is at the same distance (in units of σ) as the collimator that defines its position.

The second step consists of determining the relative position of the sensors in a RP and that of the RPs in each arm. Track segments are fitted first within each RP and then using all RPs in each arm. The relative alignment of the sensors inside a RP and of the RPs among each other is achieved by minimizing the residuals between hits and fitted tracks. The position (shift perpendicular to the beam) and rotation (about the beam axis) of each Si sensor is optimised. Thanks to the overlap between the horizontal and vertical RPs, the relative position among all sensors within a RP, and among sensors from different RPs, can be determined. The method is applied separately to several data sub-samples in order to verify the stability of the results and have control over the systematics.

Finally, the alignment of CT-PPS with respect to the beam is performed with a sample of elastic scattering events taken by the vertical RPs. This process is relatively easy to select thanks to the two anti-parallel protons in the final state. The azimuthal symmetry of elastic scattering is exploited: the LHC optics causes the elastic hit distribution in any vertical RP to have elliptical contour lines around the beam position. This symmetry is used to determine the beam location with respect to the RPs.

The uncertainty of the procedure just discussed is 5 mrad for tilts, 50 μm for horizontal shifts and 75 μm for vertical shifts.

3.2 Physics fills

The position of CT-PPS with respect to the beam needs to be redetermined for each fill. The physics fills are characterised by high intensity with only the horizontal, CT-PPS RPs inserted at much larger distances from the beam than in the alignment fill. A different procedure is thus used; it is data driven for both horizontal and vertical alignment.

The horizontal alignment is based on the assumption that the protons produced in the pp collisions at the IP have the same kinematic distributions in all fills. Given the stability of the LHC conditions (RP positions, collimator setting and beam orbit), this reflects on the distributions of the track impact points observed in the RPs. The alignment is then achieved by matching these distributions from a physics fill to those from the alignment fill. An example of this procedure is shown in Fig. 4. For this method to work, it is important to suppress the background due to secondary interactions happening between the IP and the RPs. To this end, the correlation between the horizontal hit positions in the near and far RPs is used. The total uncertainty of horizontal alignment is about 150 μm.

The vertical position of the beam with respect to the sensors is determined with a linear fit of the y coordinate of the maximum of the track impact point distribution as function of x. The fitted function is then extrapolated to $x = 0$ (horizontal beam position). This procedure can be applied since, unlike the horizontal case, the vertical maximum is within the acceptance of the horizontal RPs. Furthermore, thanks to the linear fit, effects of non-zero vertical dispersion can

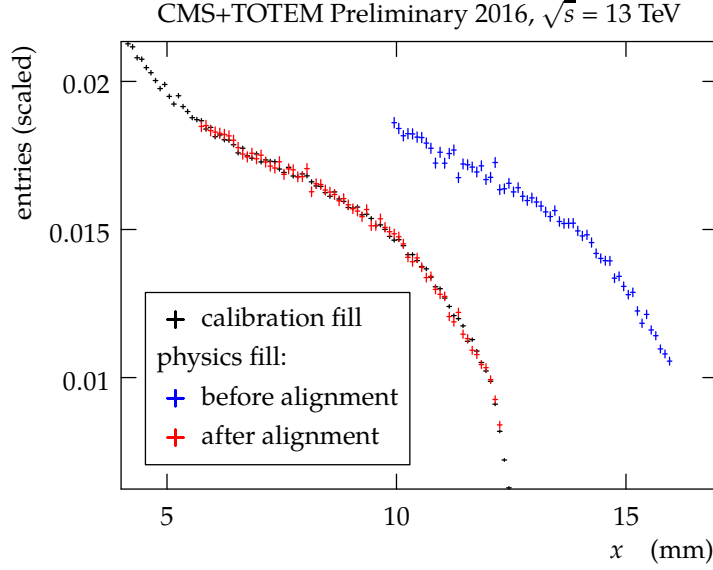CMS+TOTEM Preliminary 2016, $\sqrt{s}$ = 13 TeV

Figure 4: Distribution of the track impact points as a function of the horizontal coordinate for the alignment fill (black points), a physics fill before alignment (blue points), and after alignment (red points). The beam center is at $x = 0$ for the black and red points; the x axis origin is undefined for the blue points.

be taken into account. Here again, the resulting uncertainty is of order 150 μm.

4 LHC beam optics and proton reconstruction

The reconstruction of the scattered proton momentum from the track segments measured in the RPs requires precise knowledge of the magnetic fields traversed by the proton from the interaction point to the RPs [5]. This is normally parameterised in terms of the so-called "beam optics", in which the elements of the beam line are treated as optical lenses. The proton trajectory is described by means of transport matrices.

The trajectory of protons produced with transverse vertex position[1] (x^*, y^*) and angles (Θ_x^*, Θ_y^*) at the interaction point is described approximately by:

$$\vec{d}(s) = T(s, \xi)\vec{d}^*, \tag{1}$$

where s indicates the distance from the interaction point along the nominal beam orbit and $\vec{d} = (x, \Theta_x, y, \Theta_y, \xi)$, with

$$\xi = \Delta p / p, \tag{2}$$

and p and Δp the nominal beam momentum and the proton longitudinal momentum loss, respectively. The symbol $T(s, \xi)$ denotes the so-called single pass transport matrix, whose elements are the optical functions. The leading term in the horizontal transport is:

---

[1]The superscript '*' indicates the values at the interaction point; the absence of the superscript indicates that the values are taken at position s along the nominal beam orbit.

$$x = D_x(\xi)\xi, \tag{3}$$

where the dispersion D_x has a mild dependence on ξ. In the vertical plane, the leading term reads:

$$y \approx L_y(\xi)\Theta_y^*, \tag{4}$$

where $L_y(\xi)$ is the so-called vertical effective length. The ξ dependence of $L_y(\xi)$ is shown in Fig. 5. At any location s in the RP region, there is a value of ξ, ξ_0, where L_y vanishes and the values of y concentrate around zero. Consequently, the distribution of the track impact points exhibits a 'pinch' at $x_0 \approx D_x\xi_0$, cf. Fig. 6. The horizontal dispersion D_x can then be estimated as:

$$D_x \approx \frac{x_0}{\xi_0}. \tag{5}$$
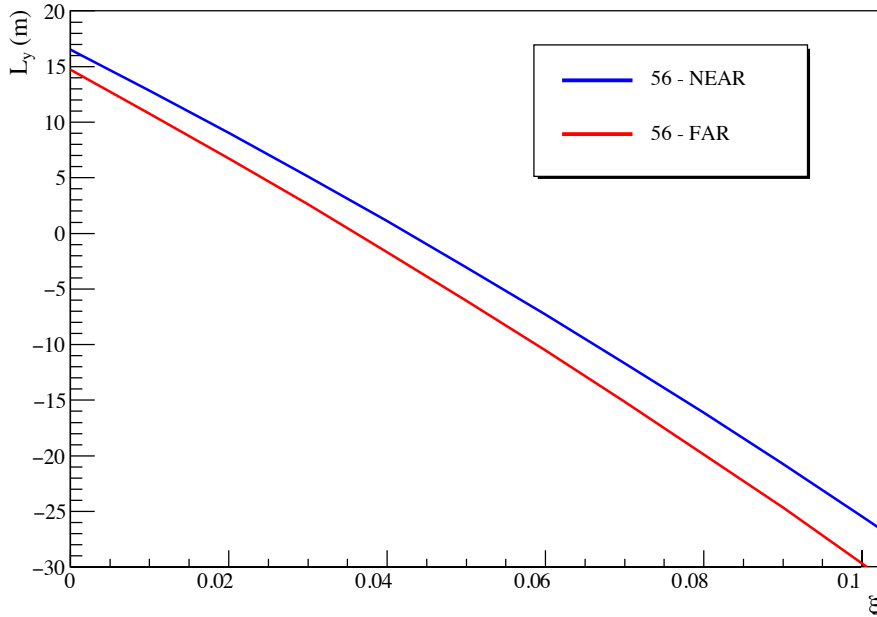
Figure 5: The vertical effective length L_y as a function of the proton momentum loss ξ at different RPs calculated with MAD-X [6].

An independent estimate of the difference of the dispersions in the two LHC beams, ΔD_x, can be obtained by means of the distribution of the protons measured in the horizontal RPs.

These two horizontal dispersion measurements and the beam position values constrain the LHC optics between the interaction point and the RPs, including the non-linearities of the proton transport matrices and notably their dependence on ξ. The optical functions are extracted with the methods originally developed for the analysis of elastic scattering data [7].

4.1   Proton reconstruction

The fractional momentum loss of a proton, ξ, can be determined from the measurements in a single RP. This is advantageous in regions where the other RP of the sector does not have suf-
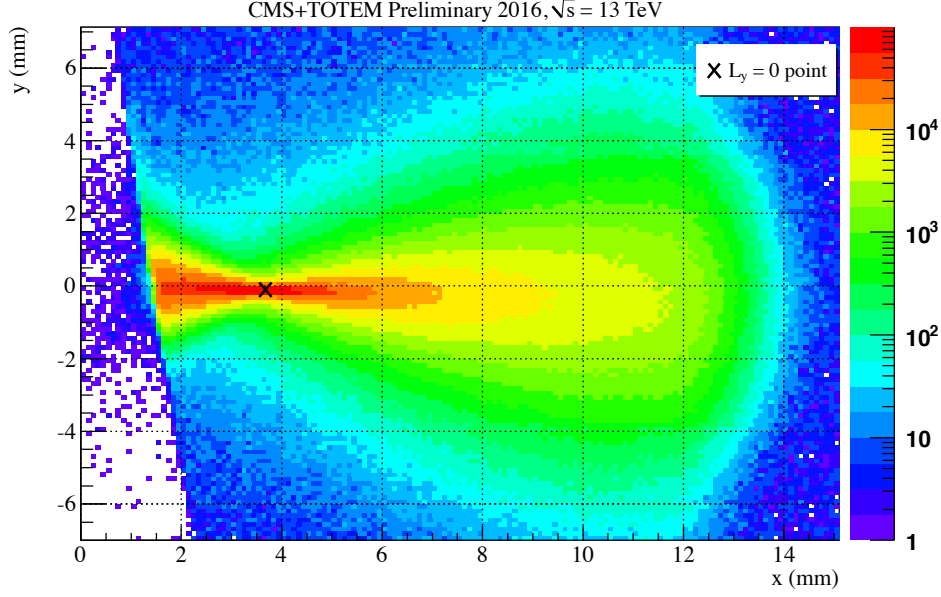
Figure 6: Distribution of the track impact points measured in RP 210F, in sector 45, in the alignment fill. The point where $L_y = 0$ and its effect in the impact point distribution are shown. The beam center is at $x = y = 0$.

ficient acceptance or is inefficient (e.g. due to radiation damage). In practice, ξ is reconstructed by inverting Eq. (3). This method ignores sub-leading terms in the proton transport (notably the one proportional to the horizontal scattering angle); their effect is included in the systematic uncertainties.

The main uncertainties are:

- dispersion calibration: relative uncertainty of D_x of about 5.5%;
- horizontal alignment: $\sigma(x) \approx 150 \ \mu$m;
- neglected terms in Eq. (3): $\sigma(x) = O(100 \ \mu$m).

For higher ξ values, the leading uncertainty comes from the dispersion.

Having reconstructed ξ, Eq. (4) can be used to determine the vertical scattering angle using the curves presented in Fig. 5. The scattering angle can in turn be related to the vertical component of the transverse momentum.

5 Data sets and Monte Carlo samples

The data used for this paper were collected from May to September 2016; they correspond to an integrated luminosity of about 10 fb^{-1}. In the same period, CMS collected a total of 15.6 fb^{-1}. After about a month the Si strip detectors suffered heavy radiation damage. After new Si-strips were installed in September, the LHC implemented a smaller crossing angle for collisions at IP5, which reflects into a different CT-PPS acceptance. These data are not used in the present analysis.

Simulated signal samples of elastic ($pp \rightarrow p\mu^+\mu^- p$) and single proton dissociative ($pp \rightarrow p\mu^+\mu^- p^*$) $\gamma\gamma \rightarrow \mu^+\mu^-$ events are produced with the LPAIR generator [8, 9], version 4.2. LPAIR is also used to produce $\gamma\gamma \rightarrow \mu^+\mu^-$ samples with both protons dissociating, $pp \rightarrow p^*\mu^+\mu^- p^*$. These three topologies are illustrated in Fig. 1. The central detector information is passed

through the standard GEANT4 [10] simulation of CMS and reconstructed as the data. Conversely, for the present analysis, the generator-level forward proton information is sufficient.

The Drell-Yan background is simulated with MADGRAPH_5_AMC@NLO [11, 12], interfaced to the CUETP8M1 tune [13] of PYTHIA 8.1 [14] for hadronization and showering.

6 Event selection

6.1 Central variables

Events were selected online by requiring the presence of two muon candidates in the CMS muon chambers with transverse momentum $p_T > 38$ GeV. No requirement on the proton was imposed online.

Offline, the two highest-p_T muons in the event are fitted to a common vertex. The vertex position from the fit is required to be consistent with that of collisions in CMS ($|z| < 15$ cm), with a $\chi^2 < 10$ ($P = 0.16\%$ for 1 degree of freedom). The muons are further required to have $p_T > 50$ GeV, to be of opposite charge, and to pass the standard CMS quality criteria [15]. No explicit isolation is required for the muons; however non-prompt muons are heavily suppressed by the track multiplicity requirement described below.

In order to select a sample enriched in $\gamma\gamma \to \mu^+\mu^-$ events, a similar procedure is used as that of the Tevatron and Run 1 LHC analyses [16–22], where no proton tagging was possible. The region around the dimuon vertex is searched for additional charged tracks, and the event is accepted if no such tracks are found within the specified veto distance. No explicit requirement is made on the p_T or the quality of these extra tracks. In addition, the dimuon acoplanarity ($a = 1 - |\Delta\phi(\mu\mu)|/\pi$) is required to be consistent with the two muons being back-to-back in ϕ. The dimuon acoplanarity as a function of the distance between the closest extra track and the dimuon vertex for the simulated signal and Drell-Yan backgrounds is shown in Fig. 7. Based on this plot, an extra-track veto region distance of at least 0.5 mm is required, along with $a < 0.009$. These cuts are looser than suggested by the simulation, reflecting the fact that the distribution of primary vertices in z is narrower in the data than in the simulation.

Finally, the invariant mass of the muons is required to be $m(\mu\mu) > 110$ GeV. This suppresses the Z-peak region, which is expected to be dominated by Drell-Yan production.

Figure 8 shows the distributions of the dimuon invariant mass and rapidity Y, after all the central detector cuts just described. The MC predictions are normalized to the total integrated luminosity. For the LPAIR predictions, "rapidity gap survival probabilities" of 0.89, 0.76 and 0.13 are applied to the elastic, the single dissociative, $pp \to p\mu^+\mu^-p^*$, and the double dissociative, $pp \to p^*\mu^+\mu^-p^*$, processes [23]. These values lead to a good description of the data at $Y = 0$, but are too large for non-zero rapidities. A Y dependence of the rapidity gap survival probability is expected in several models [24–26], but no quantitative prediction is available. A fit is therefore performed to the acoplanarity distribution in bins of Y. The Drell-Yan contribution is fixed to its nominal value, while the exclusive and dissociative LPAIR contributions are allowed to float; the single and double dissociation contributions are fitted together, i.e. their ratio is kept fixed at the LPAIR prediction. The result of the fit (not shown in the figure) suggests indeed that the rapidity gap survival probability decreases with increasing $|Y|$.

6.2 Matching central and proton variables

For each event, the value of the fractional momentum loss of the scattered proton is estimated from the muons as:
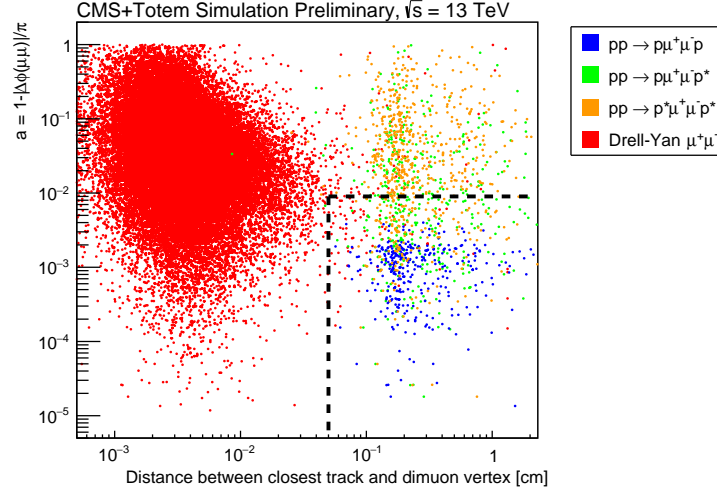
Figure 7: Dimuon acoplanarity vs the distance between the closest extra track and the dimuon vertex in signal and background simulation. The points represent the simulated Drell-Yan (red), elastic $\gamma\gamma \to \mu^+\mu^-$ (blue), single dissociative $\gamma\gamma \to \mu^+\mu^-$ (green), and double dissociative $\gamma\gamma \to \mu^+\mu^-$ (yellow) processes. The dashed lines indicate the region selected for the analysis.

$$\xi(\mu\mu) = \frac{1}{\sqrt{s}}(p_T(\mu_1)e^{\pm\eta(\mu_1)} + p_T(\mu_2)e^{\pm\eta(\mu_2)}),$$

where the two solutions for $\pm\eta$ correspond to the protons in the $\pm z$ direction.

The equation above is illustrated with simulated events in Fig. 9 in the single dissociation case, which is of interest for the present analysis. Only one of the two possible solutions will correspond to the direction of the intact proton. The formula is exact in the case in which both scattered protons are intact. However, in spite of the fact that the final state is not well known because of the proton dissociation, the correlation between the proton and $\mu^+\mu^-$ kinematics holds remarkably well, provided that the mass of the dissociating system is sufficiently small. Studies with LPAIR indicate that a mass of more than about 400 GeV is needed to produce a deviation comparable to the expected $\xi(\mu^+\mu^-)$ resolution of 3%. The latter is obtained from simulation, with an additional smearing to account for residual data-simulation differences. LPAIR also indicates that the minimum mass of the dissociating system required to generate activity in the CMS tracker is about 50 GeV; the fraction of dissociative events above this threshold is a few per cent.

To be considered as signal candidates, events are required to have a value of $\xi(\mu^+\mu^-)$ within the CT-PPS coverage; the minimum value observed in inclusive proton distributions is used. Numerically this corresponds to:

- sector 45, RP 210N: $\xi > 0.033$,
- sector 45, RP 210F: $\xi > 0.024$,
- sector 56, RP 210N: $\xi > 0.050$,
- sector 56, RP 210F: $\xi > 0.037$.

Finally, for the events with a proton predicted to be within the acceptance, the signal region is defined by requiring $\xi(\mu\mu)$ and the corresponding value measured with CT-PPS, $\xi(RP)$, to
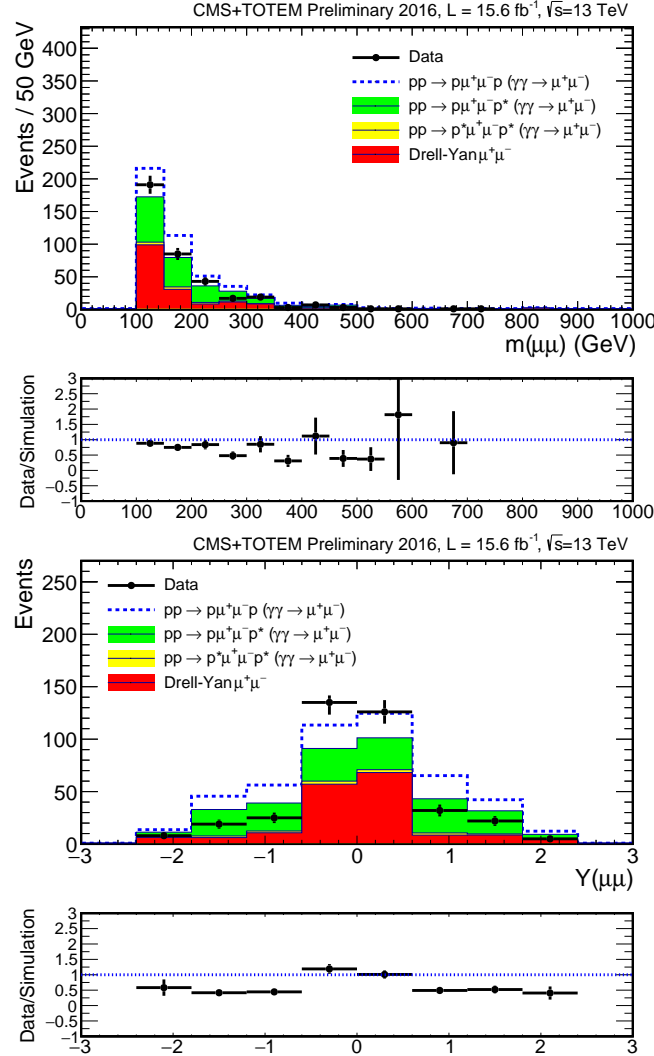
Figure 8: Dimuon invariant mass (above) and rapidity (below), after all central detector selection cuts. The lower panel in each plot shows the ratio of the data to the sum of all signal and background predictions.

match within 2σ of their combined uncertainty.

7   Background

After the selection illustrated above, the backgrounds are expected to arise mainly from prompt $\mu^+\mu^-$ production combined with proton tracks from unrelated pileup interactions or beam backgrounds in the same bunch crossing. The largest sources of prompt $\mu^+\mu^-$ production without leading protons are the Drell-Yan process, and $\gamma\gamma \to \mu^+\mu^-$ production in which both protons dissociate.

To estimate both the Drell-Yan and the dissociative backgrounds, a control sample of $Z \to \mu^+\mu^-$ events is used. To avoid statistical correlation between the two estimates, only every second event from the sample is considered for the Drell-Yan estimate, and the remaining part for the double-dissociative background. In both cases, the background estimation is mostly data driven, and does not require the detailed knowledge of the RP acceptance and detector
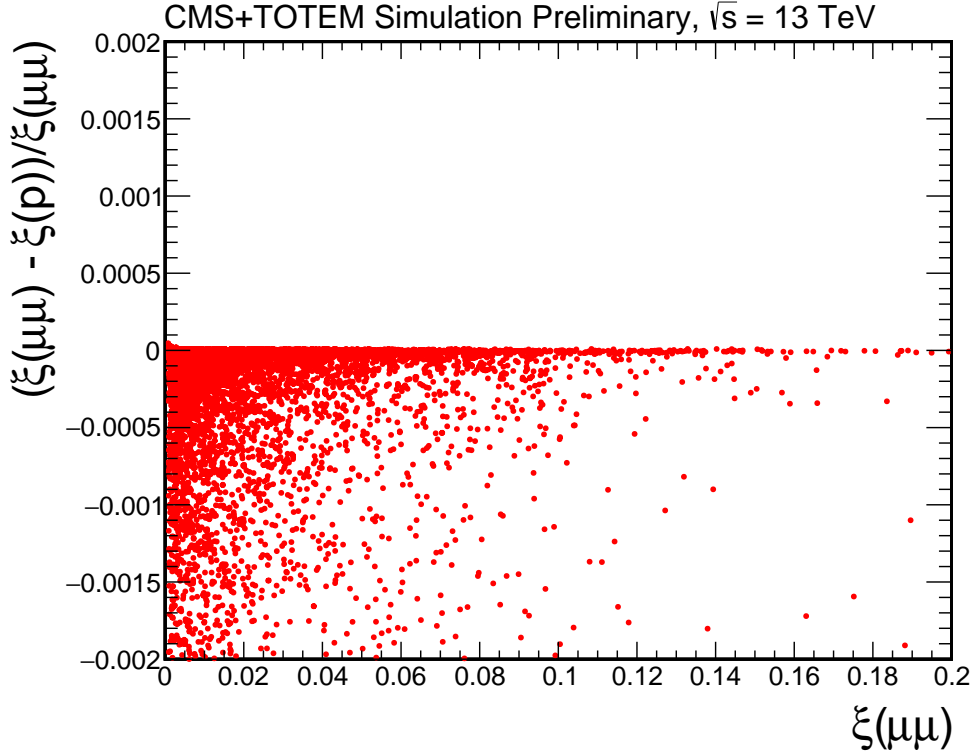
Figure 9: Generator-level relative difference $\frac{\xi(\mu\mu)-\xi(p)}{\xi(\mu\mu)}$ vs. $\xi(\mu\mu)$ for single dissociative $\gamma\gamma \rightarrow \mu^+\mu^-$ production. Of the two possible solutions for $\xi(\mu\mu)$, only the one corresponding to the side with the intact proton is shown.

efficiency. The procedure is illustrated in the following:

- In order to estimate the Drell-Yan background, the track multiplicity and acoplanarity selection criteria are not applied, and an invariant mass window of $80 < m(\mu\mu) < 110$ GeV is imposed, resulting in a high purity sample of Drell-Yan events. A subsample is then selected with a proton track matching the kinematics of the $\mu^+\mu^-$ pair. However, the Drell-Yan events in this subsample tend to be concentrated at mid-rapidity, which causes a distortion of the $\xi(\mu^+\mu^-)$ distribution. The distribution is therefore reweighted so as to have the shape predicted by the Drell-Yan simulation. Finally, the simulated Drell-Yan sample is used to extrapolate to the number of background events expected in the signal region.

- The background from $\gamma\gamma \rightarrow \mu^+\mu^-$ production with double dissociation is estimated by mixing simulated double dissociation events with proton information from the Z sample mentioned above. The protons from this sample are used for convenience, but any other sample of protons would be fine; the information from the central part of the event is not used.

  The Monte Carlo events passing the central detector cuts are selected, and an exponential function is fitted to the corresponding $\xi(\mu\mu)$ distribution. Then a toy simulation is performed in which the fit is sampled, and the value of $\xi(\mu\mu)$ is randomly assigned to a proton from the Z sample.

  The background estimate is obtained as the number of events in the toy simulation

Arm	1σ	2σ	3σ	full
Left	0.373 ± 0.034	0.752 ± 0.048	1.054 ± 0.057	6.135 ± 0.132
Right	0.319 ± 0.031	0.610 ± 0.043	0.850 ± 0.050	4.444 ± 0.111

Table 1: Estimated backgrounds from Drell-Yan production, with proton kinematics matching within 1σ, 2σ, 3σ, and within the full acceptance range in at least one of the FAR and NEAR Roman Pots of a given arm.

Arm	1σ	2σ	3σ	full
Left	0.028 ± 0.003	0.046 ± 0.003	0.072 ± 0.004	0.572 ± 0.012
Right	0.027 ± 0.002	0.059 ± 0.004	0.087 ± 0.005	0.482 ± 0.011

Table 2: Estimated backgrounds from double-dissociation $\gamma\gamma \rightarrow \mu\mu$ production, with proton kinematics matching within 1σ, 2σ, 3σ, and within the full acceptance range in at least one of the FAR and NEAR Roman Pots of a given arm.

> that pass the proton selection (cf. Section 6.2) in addition to the central cuts, normalized to the number of Monte Carlo events passing the central signal selection. The procedure just described forces all double dissociation events to have a background proton in CT-PPS. The background estimate thus needs to be scaled by the fraction of events passing the central selection that do not have a proton in CT-PPS. This is obtained from the data.
>
> For the simulation of the double dissociation process, the Y-independent rapidity gap survival probability of 0.13 quoted above is used. If instead the results of the fit discussed in Section 6 were used, the dissociative backround estimate would decrease by a factor about five, and the total background by 6%. The present estimate is thus conservative.

- Since baryon number is conserved, the dissociating system may contain a final state proton that falls within the CT-PPS acceptance, even without overlap of an unrelated proton. However, the simulation indicates that the total number of such events within the acceptance is expected to be < 1, and the number with matching $\xi(\mu^+\mu^-)$ and $\xi(\text{RP})$ is negligible.

In order to compare the background estimates with the data, the numbers of background events expected with tracks in either or both of the near and far RPs in each arm have been evaluated. These are shown in Tables 1 and 2. For a 2σ matching window, the total background prediction is 1.47 ± 0.06 (stat.) events with a matching track in at least one RP, in both arms combined. An additional 10.2 ± 0.2 (stat.) are expected within the acceptance, but falling outside the 2σ matching window.

The systematic uncertainties in the Drell-Yan and double dissociation background are estimated as follows. A 5% contribution is included reflecting the statistical uncertainty of the control sample of protons from the Z-peak region. In addition, the Drell-Yan background estimate is affected by uncertainties related to the reweighting of the $\xi(\mu^+\mu^-)$ distribution and the modelling of the track multiplicity distribution in the simulation. The former is obtained as the difference of the background estimates with and without reweighting, leading to a 25% relative uncertainty. The latter is estimated from the difference between data and simulation in the low multiplicity region, with 1-5 additional tracks near the dimuon vertex, resulting in a 28% relative uncertainty. The double dissociation background estimate also includes a 100% relative uncertainty on the rapidity gap survival probability. Finally, the double dissociation background includes a 2.5% luminosity uncertainty [27], resulting from the normalization of

the simulated samples.

As a further check of the background estimate, a toy experiment is performed in which the measured values of $\xi(\mu\mu)$ within the CT-PPS acceptance are randomly coupled with values of $\xi(p)$ from events without any offline selection imposed on the central variables. The dimuon system and the proton originate from different events and are thus uncorrelated. The toy experiment is repeated 10^4 times, and the average number of events in which $\xi(\mu\mu)$ and $\xi(p)$ match within 2σ is determined. The result is consistent with the background estimate of 1.47 ± 0.06 (stat.) events discussed above.

8 Results

Figure 10 shows the correlation between $\xi(RP)$ and $\xi(\mu^+\mu^-)$. In total 17 events are observed with a $\xi(\mu^+\mu^-)$ within the CT-PPS acceptance, and at least one track detected in the relevant RPs. Five of those events have a mismatch of $\geq 2\sigma$ between the dimuon and the proton kinematics, compared to 10.2 ± 3.6 (stat. + syst.) such events expected from the background studies discussed in Section 7. Twelve events have a track in at least one of the two RPs matching $\xi(\mu^+\mu^-)$ within 2σ. The significance of observing 12 events over the background estimate of 1.47 ± 0.06 (stat.) ± 0.52 (syst.), including the systematic uncertainties as log-normal nuisance parameters, is 4.3σ.
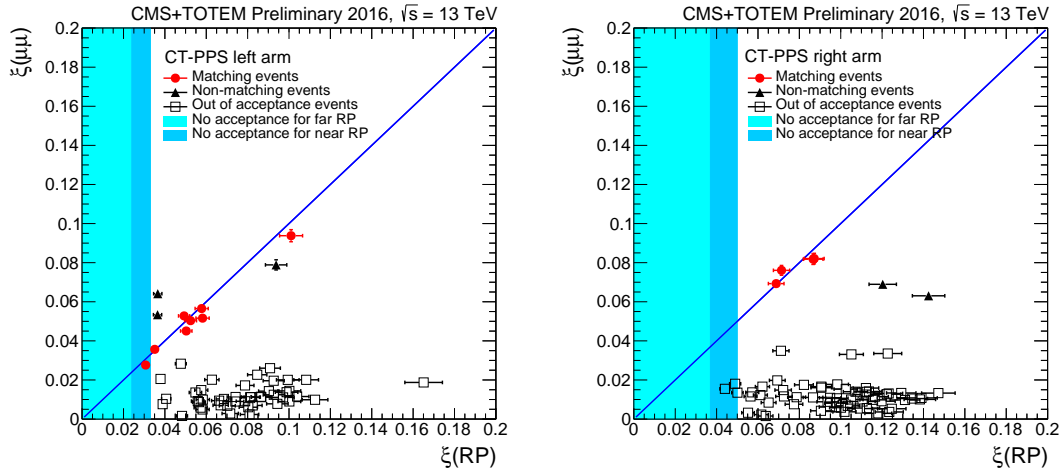
Figure 10: Correlation between $\xi(\mu\mu)$ and ξ measured in the Roman Pots, for both Roman Pots in each arm combined. The 45 (left) and 56 (right) arms are shown. The light shaded region corresponds to the kinematical region outside the acceptance of both the near and far RPs, while the darker shaded region corresponds to the region outside the acceptance of the near RP. For the events in which a track is detected in both, the ξ value measured at the near RP is plotted.

The distribution of the matching events in the space of dimuon mass-rapidity is shown in Fig. 11. The candidate events are consistent with the expected acceptance for detecting protons in a single arm, given the LHC optics and the position of the Roman Pots. No events are observed with matching protons in both arms; the highest-mass event is at $m(\mu\mu) = 342$ GeV, approximately 20 GeV below the threshold required to detect both protons.

Central semi-exclusive dimuon events are expected to have very small values of $|t|$, the absolute value of the four-momentum squared exchanged at the proton vertices. For the present
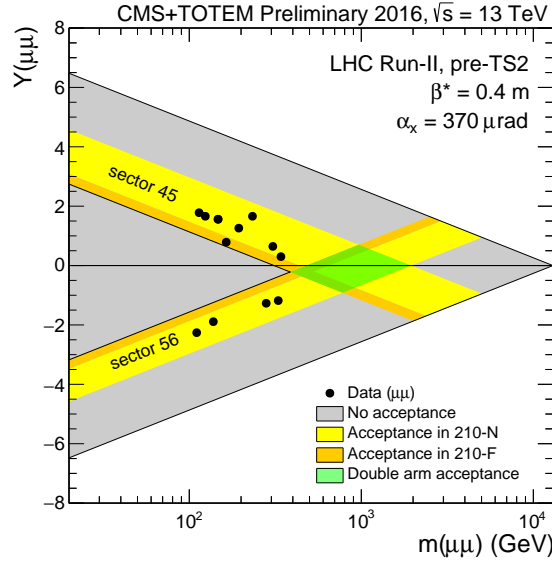
Figure 11: Expected coverage in the rapidity vs invariant mass plane overlaid with the observed dimuon signal candidate events. Following the CMS convention, the positive rapidity (negative rapidity) region corresponds to the 45 (56) LHC sector.

data, only the vertical component of the scattering angle, and hence of the proton transverse momentum, is measured. For 11 candidate events out of the 12, the vertical component of the scattering angle is compatible with zero within at most 2.5σ, where σ is the uncertainty of the vertical component of the scattering angle. For one event, the discrepancy is 3.5σ, in agreement with the background estimate.

9   Summary

We have studied $\gamma\gamma \rightarrow \mu^+\mu^-$ production with forward protons reconstructed in the CMS-TOTEM Precision Proton Spectrometer, using a sample of about 10 fb^{-1} collected in high luminosity LHC data taking at 13 TeV. The Roman Pot alignment and LHC optics corrections have been derived using a high statistics sample of forward protons. A total of 12 $\gamma\gamma \rightarrow \mu^+\mu^-$ candidates with $m(\mu\mu) > 110$ GeV, and matching forward proton kinematics, is observed. This corresponds to an excess larger than four standard deviations over the background. The result confirms the reliability of the alignment and optics determination, and represents the first evidence for proton-tagged $\gamma\gamma$ collisions at the electroweak scale. The present data demonstrate the excellent performance of CT-PPS and its potential. With its 2016 operation, CT-PPS has proven for the first time the feasibility of operating a near-beam proton spectrometer at a high luminosity hadron collider on a regular basis.

Acknowledgments

References

[1] CMS Collaboration, "The CMS experiment at the CERN LHC", *JINST* **3** (2008) S08004, `doi:10.1088/1748-0221/3/08/S08004`.

[2] M. Albrow et al., "CMS-TOTEM Precision Proton Spectrometer", Technical Report CERN-LHCC-2014-021. TOTEM-TDR-003. CMS-TDR-13, 2014.

[3] TOTEM Collaboration, "Performance of the TOTEM Detectors at the LHC", *Int. J. Mod. Phys.* **A28** (2013) 1330046, `doi:10.1142/S0217751X13300469`, `arXiv:1310.2908`.

[4] J. Kaspar, "Alignment of CT-PPS detectors in 2016, before TS2", CERN-TOTEM-NOTE-2017-001, 2017.

[5] F. Nemes, "LHC optics determination with proton tracks measured in the CT-PPS detectors in 2016, before TS2", CERN-TOTEM-NOTE-2017-002, 2017.

[6] H. Grote and F. Schmidt, "MAD-X: An upgrade from MAD8", *Conf.Proc.* **C030512** (2003) 3497.

[7] TOTEM Collaboration, "LHC Optics Measurement with Proton Tracks Detected by the Roman Pots of the TOTEM Experiment", *New J. Phys.* **16** (2014) 103041, `doi:10.1088/1367-2630/16/10/103041`, `arXiv:1406.0546`.

[8] J. A. M. Vermaseren, "Two Photon Processes at Very High Energies", *Nucl. Phys.* **B229** (1983) 347–371, `doi:10.1016/0550-3213(83)90336-X`.

[9] S. P. Baranov, O. Duenger, H. Shooshtari, and J. A. M. Vermaseren, "LPAIR: A generator for lepton pair production", in *Workshop on Physics at HERA Hamburg, Germany, October 29-30, 1991*, pp. 1478–1482. 1991.

[10] GEANT4 Collaboration, "GEANT4: A Simulation toolkit", *Nucl. Instrum. Meth.* **A506** (2003) 250–303, `doi:10.1016/S0168-9002(03)01368-8`.

[11] J. Alwall et al., "The automated computation of tree-level and next-to-leading order differential cross sections, and their matching to parton shower simulations", *JHEP* **07** (2014) 079, `doi:10.1007/JHEP07(2014)079`, `arXiv:1405.0301`.

[12] R. Frederix and S. Frixione, "Merging meets matching in MC@NLO", *JHEP* **12** (2012) 061, `doi:10.1007/JHEP12(2012)061`, `arXiv:1209.6215`.

[13] CMS Collaboration, "Event generator tunes obtained from underlying event and multiparton scattering measurements", *Eur. Phys. J.* **C76** (2016), no. 3, 155, `doi:10.1140/epjc/s10052-016-3988-x`, `arXiv:1512.00815`.

[14] T. Sjöstrand, S. Mrenna, and P. Z. Skands, "A Brief Introduction to PYTHIA 8.1", *Comput. Phys. Commun.* **178** (2008) 852–867, `doi:10.1016/j.cpc.2008.01.036`, `arXiv:0710.3820`.

[15] CMS Collaboration, "Performance of CMS muon reconstruction in pp collision events at $\sqrt{s} = 7$ TeV", *JINST* **7** (2012) P10002, `doi:10.1088/1748-0221/7/10/P10002`, `arXiv:1206.4071`.

[16] CMS Collaboration, "Evidence for exclusive $\gamma\gamma \to W^+W^-$ production and constraints on anomalous quartic gauge couplings in pp collisions at $\sqrt{s} = 7$ and 8 TeV", *JHEP* **08** (2016) 119, `doi:10.1007/JHEP08(2016)119`, `arXiv:1604.04464`.

[17] CMS Collaboration, "Study of exclusive two-photon production of W^+W^- in pp collisions at $\sqrt{s} = 7$ TeV and constraints on anomalous quartic gauge couplings", *JHEP* **07** (2013) 116, `doi:10.1007/JHEP07(2013)116`, `arXiv:1305.5596`.

[18] CMS Collaboration, "Exclusive photon-photon production of muon pairs in proton-proton collisions at $\sqrt{s} = 7$ TeV", *JHEP* **01** (2012) 052, `doi:10.1007/JHEP01(2012)052`, `arXiv:1111.5536`.

[19] ATLAS Collaboration, "Measurement of exclusive $\gamma\gamma \to W^+W^-$ production and search for exclusive Higgs boson production in pp collisions at $\sqrt{s} = 8$ TeV using the ATLAS detector", *Phys. Rev.* **D94** (2016), no. 3, 032011, `doi:10.1103/PhysRevD.94.032011`, `arXiv:1607.03745`.

[20] ATLAS Collaboration, "Measurement of exclusive $\gamma\gamma \to \ell^+\ell^-$ production in proton-proton collisions at $\sqrt{s} = 7$ TeV with the ATLAS detector", *Phys. Lett.* **B749** (2015) 242–261, `doi:10.1016/j.physletb.2015.07.069`, `arXiv:1506.07098`.

[21] CDF Collaboration, "Search for exclusive Z boson production and observation of high mass $p\bar{p} \to \gamma\gamma \to p + \ell\ell + \bar{p}$ events in $p\bar{p}$ collisions at $\sqrt{s} = 1.96$ TeV", *Phys. Rev. Lett.* **102** (2009) 222002, `doi:10.1103/PhysRevLett.102.222002`, `arXiv:0902.2816`.

[22] CDF Collaboration, "Observation of exclusive charmonium production and $\gamma + \gamma$ to $\mu^+\mu^-$ in $p\bar{p}$ collisions at $\sqrt{s} = 1.96$ TeV", *Phys. Rev. Lett.* **102** (2009) 242001, `doi:10.1103/PhysRevLett.102.242001`, `arXiv:0902.1271`.

[23] L. A. Harland-Lang, V. A. Khoze, and M. G. Ryskin, "The photon PDF in events with rapidity gaps", *Eur. Phys. J.* **C76** (2016), no. 5, 255, `doi:10.1140/epjc/s10052-016-4100-2`, `arXiv:1601.03772`.

[24] M. Dyndal and L. Schoeffel, "The role of finite-size effects on the spectrum of equivalent photons in protonproton collisions at the LHC", *Phys. Lett.* **B741** (2015) 66–70, `doi:10.1016/j.physletb.2014.12.019`, `arXiv:1410.2983`.

[25] L. A. Harland-Lang, V. A. Khoze, and M. G. Ryskin, "Exclusive physics at the LHC with SuperChic 2", *Eur. Phys. J.* **C76** (2016), no. 1, 9, `doi:10.1140/epjc/s10052-015-3832-8`, `arXiv:1508.02718`.

[26] P. Lebiedowicz and A. Szczurek, "Exclusive production of heavy charged Higgs boson pairs in the $pp \to ppH^+H^-$ reaction at the LHC and a future circular collider", *Phys. Rev.* **D91** (2015) 095008, `doi:10.1103/PhysRevD.91.095008`, `arXiv:1502.03323`.

[27] CMS Collaboration Collaboration, "CMS Luminosity Measurements for the 2016 Data Taking Period", Technical Report CMS-PAS-LUM-17-001, CERN, Geneva, 2017.